Nuclear Materials and Energy 38 (2024) 101602

Contents lists available at ScienceDirect

Nuclear Materials and Energy

journal homepage: www.elsevier.com/locate/nme

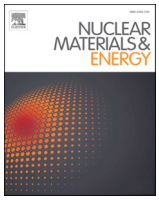

Effect of the heating rate and Y_2O_3 coating on the microstructure of W_f/Y_2O_3/W composites via field assisted sintering technology

Rui Shu [a,b,*], Yiran Mao [a], Alexander Lau [a], Jan W Coenen [a,d], Alexis Terra [a], Chao Liu [b], Johann Riesch [c], Christian Linsmeier [a], Christoph Broeckmann [b]

[a] Forschungszentrum Jülich GmbH, Institut für Energie- und Klimaforschung - Plasmaphysik, Partner in the Trilateral Euregio Cluster, 52425 Jülich, Germany
[b] Institut für Werkstoffanwendungen im Maschinenbau (IWM), RWTH Aachen University, 52062 Aachen, Germany
[c] Max-Planck-Institut für Plasmaphysik, 85748 Garching b. München, Germany
[d] Department of Nuclear Engineering & Engineering Physics, University of Wisconsin Madison, Madison, WI 53706 Madison, USA

ARTICLE INFO

Keywords:
W_f/Y_2O_3/W composites
Heating rate
Y_2O_3 coating
Microstructure
Field assisted sintering technology

ABSTRACT

Field assisted sintering technology (FAST) is one of the potential methods to fabricate tungsten fiber reinforced tungsten (W_f/W) composites. The microstructure and mechanical properties of W_f/W composites are closely related to the sintering parameters. In the present work, the W_f/W composites with a Y_2O_3 coating on the fiber (W_f/Y_2O_3/W) were fabricated via a FAST process and the microstructure was characterized. The influence of the heating rate and Y_2O_3 coating on the microstructure of W_f/Y_2O_3/W composites was discussed in detail. It is observed that the Y_2O_3 coating can get damaged and move into the adjacent matrix. A higher heating rate (100 ℃/min) causes more serious damage on the Y_2O_3 coating which could be attributed to the higher electric current intensity. The samples produced with a lower heating rate (50 ℃/min) or with a thicker Y_2O_3 coating (3 μm) show an interface with better continuity. In addition, the integrity of the Y_2O_3 coating could by protected by an additional W-coating produced by chemical vapor deposition (CVD).

1. Introduction

Tungsten fiber reinforced tungsten (W_f/W) composites are one of the promising solutions to overcome the poor toughness of tungsten below ductile to brittle transition temperature (DBTT) [1–4]. W_f/W composites are developed based on the extrinsic toughening mechanisms similar to the fiber reinforced ceramic composites [5–7] and show a pseudo-ductile behavior during the fracture process [8–10].

The potassium-doped tungsten fibers (W_f) have a great ductility due to the high aspect ratio of the grains, while the strength and ductility of the fiber may decrease after annealing because of recrystallization and grain growth [11–14]. The W_f/W composites are commonly consolidated under a high temperature sintering by using powder metallurgy methods [15–17], such as hot pressing (HP), hot isostatic pressing (HIP) and field assisted sintering technology (FAST, also known as spark plasma sintering (SPS)), leading to the similar effect of annealing. In particular, FAST has the effect of a pulsed electric current in addition to the high temperature and high pressure [18,19]. The previous research about the effect of sintering parameters on W_f/W composites are mainly focused on the temperature and pressure. Nevertheless, the heating rate is also one of the important sintering parameters and can affect the microstructure of the samples [20,21].

In addition, many studies have proven that the extrinsic toughening mechanisms in fiber reinforced composites rely on the weak fiber–matrix interface [22–24]. In order to achieve a suitable fiber–matrix interface, various interface materials have been investigated [25–27], such as Cu, Er_2O_3 and Y_2O_3, as well as a porous tungsten matrix have been considered to get a weak boundary [28,29]. Y_2O_3 shows positive effects on improving the ductility of W-based materials due to its good thermal and chemical stability, high mechanical strength and hardness [30,31]. The Y_2O_3 film produced by reactive sputtering shows high compactness and stability that makes it suitable as a fiber–matrix interface layer [32,33]. Apart from being the weak interface, Y_2O_3 coatings also play a role to protect the microstructure of the fibers during the FAST process [34]. However, there is only few literature regarding the effect of the Y_2O_3 coating on the microstructure of the composites. Moreover, based on previous studies [5,16,34], FAST process damages the integrity of the Y_2O_3 interface, potentially due to the

* Corresponding author.
E-mail address: r.shu@fz-juelich.de (R. Shu).

https://doi.org/10.1016/j.nme.2024.101602
Received 10 December 2023; Received in revised form 18 January 2024; Accepted 29 January 2024
Available online 1 February 2024

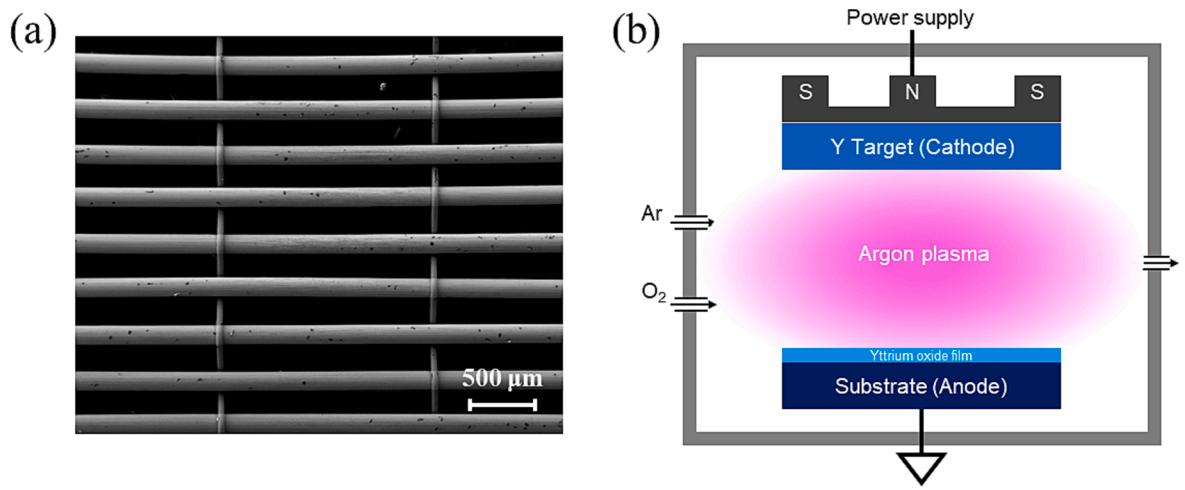

Fig. 1. (a) The W_f weave [34]; (b) Schematic diagram of the Y_2O_3 coating process by magnetron sputtering.

high temperature, pressure and current. Therefore, it is hard to achieve an intact interface utilizing the powder metallurgical preparation.

In the present work, $W_f/Y_2O_3/W$ composites were fabricated via magnetron sputtering and FAST under different Y_2O_3 coating states and heating rates during sintering. The microstructure of the prepared $W_f/Y_2O_3/W$ composites were characterized and the differences between each sample were discussed in detail. The goal is to find out a process route that enhances the integrity of the fiber–matrix interface beyond the current state after the FAST process.

2. Experimental

2.1. Y_2O_3 coating preparation

The as-fabricated K-doped tungsten fibers [13,35] (W_f, with a diameter of 150 μm) were used as the raw material. The grains along the drawing direction are extremely elongated. Perpendicular to the drawing axis, the grains have significantly smaller dimensions and are twisted forming a characteristic curled structure [35]. These fibers were further fabricated into W_f weaves (Fig. 1a), utilizing a Mageba shuttle loom (type SL 1/80) textile machine, with a warp fiber distance of 0.2 mm, and weft fibers with a smaller diameter (50 μm) and a distance of 2 mm. These weft fibers were mainly used to fix the warp fibers position [36]. The W_f weaves were cut into a round shape of 40 mm diameter to fit the sintering mold and coated with a layer of Y_2O_3 by a Prevac magnetron sputtering system (Fig. 1b). The magnetron target material was yttrium metal (Kurt J. Lesker Company, 99.9% purity, 76.2 mm diameter, 6.35 mm thickness). During the magnetron sputtering process, a constant argon (Ar) gas flow of 25 standard cubic centimeter per minute (sccm) is injected at the target position to generate the plasma and the oxygen with a flow between 2 sccm and 10 sccm is injected as the reactive gas. Due to the limitations of the magnetron sputtering device, the coating process was carried out side by side. After the deposition of the first side, the fabrics were manually flipped to deposit the second side. More coating details are similar to the process described in [33]. Two different coating times of 70 min and 90 min were used to deposit the Y_2O_3 coating of different thicknesses (1.6 μm and 3 μm). After that, half of the W_f weaves with 3 μm Y_2O_3 coating were coated with a layer of pure W for protection by chemical vapor deposition (CVD, the process was as described in [8,37]). The temperature for the process was at 420 ℃ at a pressure of 100 mbar and a coating time of 8 min with a preheating temperatures at 600 °C and a preheating retention time of approx. 1.5 s. The gas flow rate was 8750 sccm for H_2 and 700 sccm for WF_6, respectively.

2.2. $W_f/Y_2O_3/W$ composites fabrication

The samples were assembled into the graphite mold (with a diameter of 40 mm) by placing one layer of W powder (with the average particle size of 5 μm) and one layer of W_f weave alternately (totaling with 19 layers of W powders and 18 layers of W_f weaves) [38]. Each layer of W powder was 4.5 g and all the W_f weaves are oriented unidirectionally. Two layers of tungsten sheet were used to separate the sample and graphite sheets (aiming to reduce the damage of the mold surface and to ease the sample removal process) in order to reduce the carbon contamination [34]. The samples were consolidated via a commercial FAST system (HP D 25-2) from "FCT Systeme GmbH" (max force, 250 kN; max temperature, 2200 ℃; max heating rate, 400 K/min). Table 1 shows the fabrication parameters of the $W_f/Y_2O_3/W$ composites. All samples have the same sintering temperature of 1800 ℃ and a 5 min holding time under 50 MPa. The heating rate of the sample $WY_{1.6}W\_100$ is 100 ℃/min and the other samples have the heating rate of 50 ℃/min. Fig. 2a illustrates the FAST process and Fig. 2b shows the evolution of temperature and pressure with time at different heating rates. The evolution of the pressure is related to the heating rate and all samples have the same cooling rate of ≈375 ℃/min.

2.3. Characterization

The density of the sintered samples were measured via a Sartorius Cubis MSA225S precision balance (Sartorius AG, Göttingen) with the fluid medium of pure Ethanol (99.5%) according to the Archimedes principle. The microstructure of the coated fibers and the sintered composites was analyzed via a Carl Zeiss LEO DSM 982 scanning

Table 1
Fabrication parameters of the $W_f/Y_2O_3/W$ composites.

Samples	Thickness of Y_2O_3 coating (μm)	Heating rate (℃/min)	Temperature (℃)	Pressure (MPa)	Holding time (min)
$WY_{1.6}W\_100$	1.6	100	1800	50	5
$WY_{1.6}W\_50$	1.6	50			
WY_3W_50	3	50			
$WY_3W\_W\_50$	3 + CVD-W layer	50			

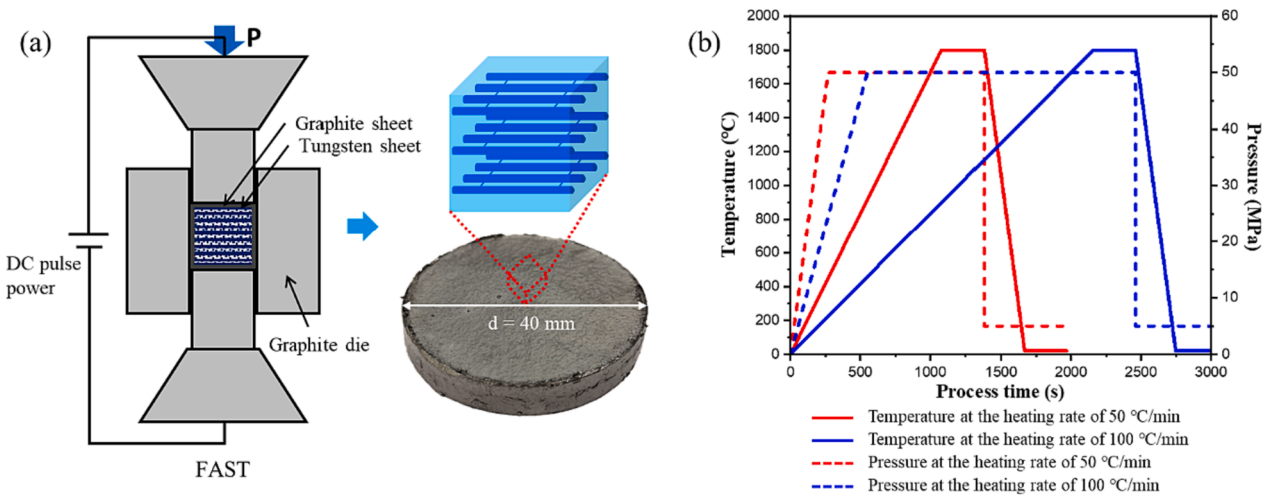

Fig. 2. (a) Schematic diagram of the FAST process [34]; (b) Temperature-time and pressure–time curves of the FAST process during the production.

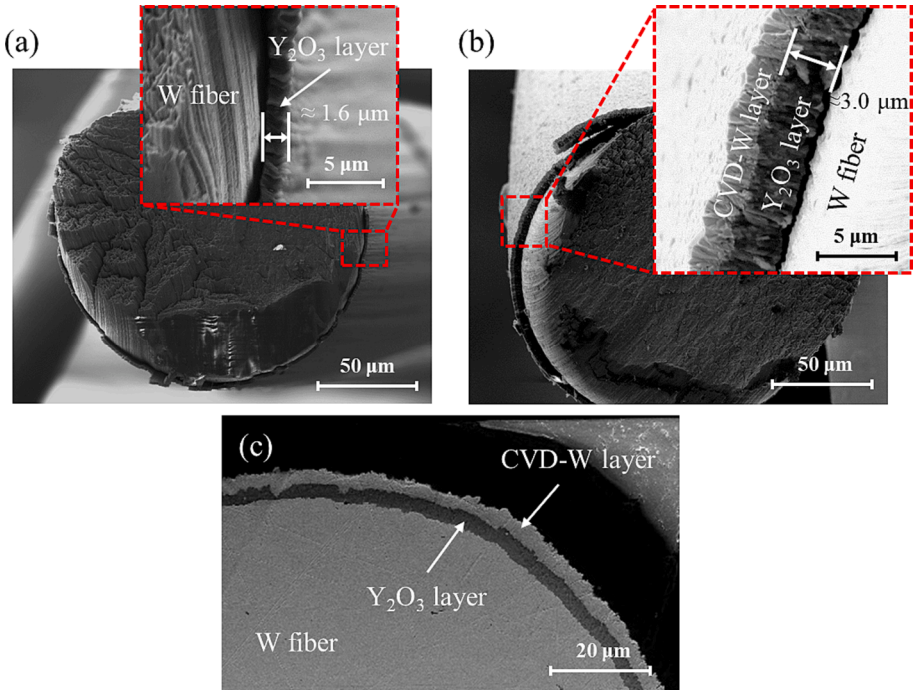

Fig. 3. SEM images of the fibers with Y_2O_3 coating: (a) 1.6 μm thick coating; (b, c) 3 μm thick coating with a layer of CVD-W.

electron microscope (SEM, Jena, Germany) with an energy dispersive X-ray spectroscopy (EDX, Oxford Instruments, operated at 10 kV) system after mechanical polishing and polishing with oxide polishing suspension (OPS). The grain size of the fibers was statistically analyzed by measuring the diameter of the grains and the distribution of each element at the interface was characterized by EDX.

3. Results and discussion

Fig. 3 reveals the morphology of the fibers after Y_2O_3 coating. The cross-sections were obtained by cutting the fibers with a scissor, so a slight separation between the fiber and Y_2O_3 layer could be observed. The original boundary between the fiber and Y_2O_3 coating is in tight contact without gap, which is similar to the report in [33]. The microstructure of the Y_2O_3 layers under for both coating times are dense and uniform. The thickness of the Y_2O_3 layer obtained by 70 min coating is ≈1.6 μm (Fig. 3a) and a ≈3 μm Y_2O_3 layer is obtained after 90 min coating. For the $WY_3W\_W\_50$ sample, a protection layer of CVD-W (with the thickness of 2–5 μm) is tightly covered on the Y_2O_3 coating (as shown in Fig. 3b and c).

Fig. 4 shows the microstructure of the sintered $W_f/Y_2O_3/W$ composites. The samples have the same volume fraction of the fiber (≈20%) and the fibers are uniformly distributed in the matrix, while there are some differences in the distribution of fibers in various samples due to the samples being manually assembled. There is no observable interlayer existing between the fibers and the matrix of $WY_{1.6}W\_100$ (as shown in Fig. 4a), which means the Y_2O_3 coating has been completely lost during the FAST process. In contrast, a clear interlayer can be observed in the other three samples (Fig. 4b and c), although the integrity of the interlayer in each sample is different (by observing and measuring the proportion of the interlayer phase in the fiber–matrix interface zone). The microstructure of the interlayer in $WY_{1.6}W\_W\_50$ shows the highest integrity.

In addition, the fibers have the uniform equiaxed grains in the cross-

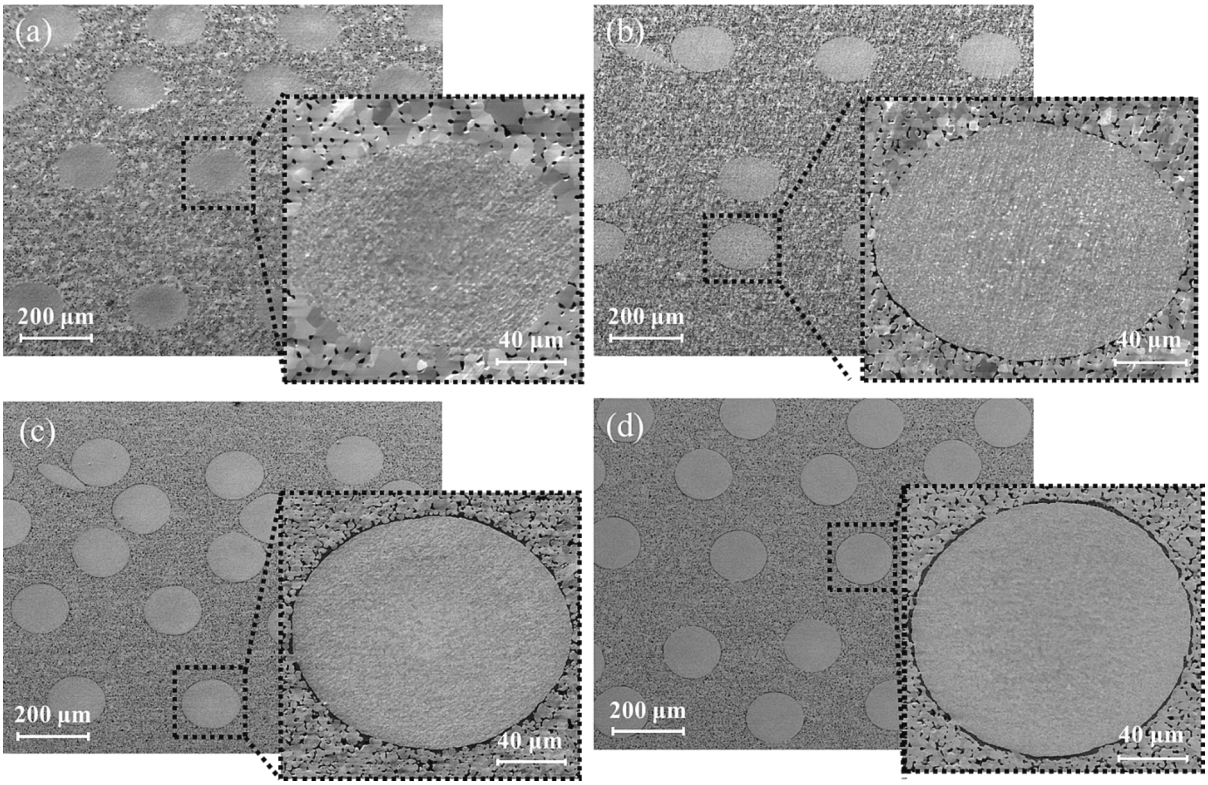

Fig. 4. Microstructure of the $W_f/Y_2O_3/W$ composites (in the cross-section of fibers): (a) $WY_{1.6}W\_100$; (b) $WY_{1.6}W\_50$; (c) WY_3W_50; (d) $WY_3W\_W\_50$.

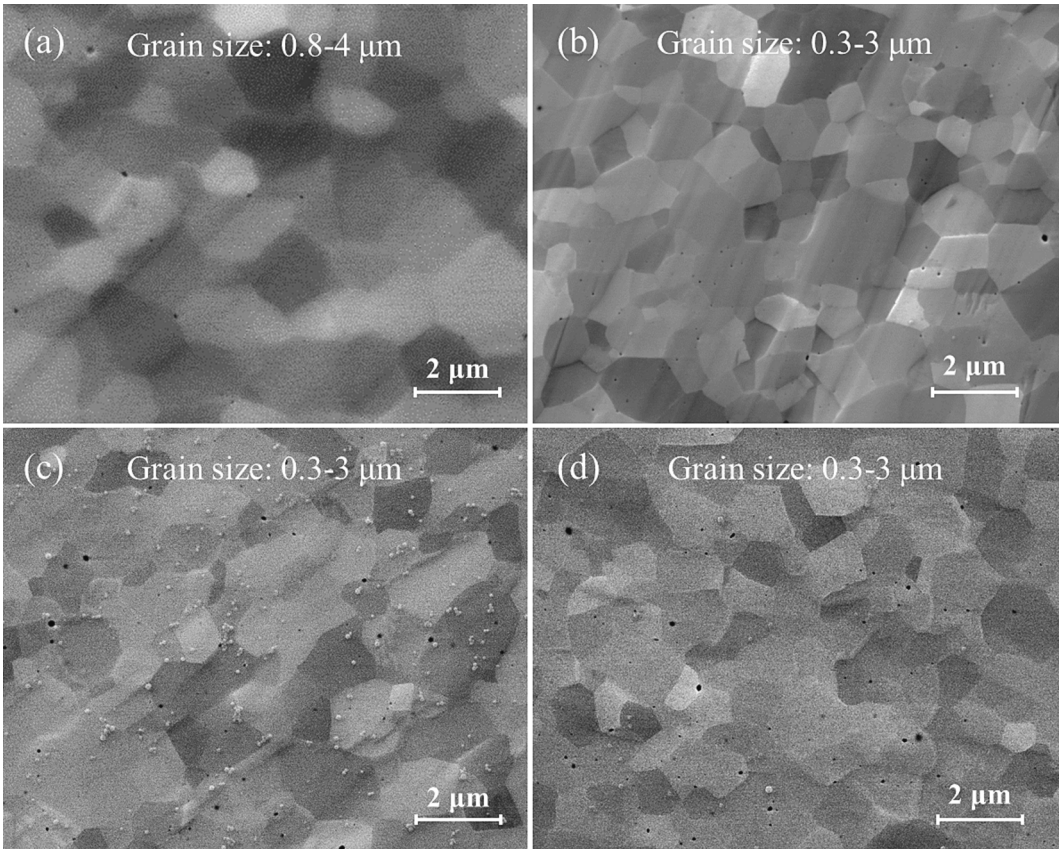

Fig. 5. The grains in the cross-section of the fiber in $W_f/Y_2O_3/W$ composites: (a) $WY_{1.6}W\_100$; (b) $WY_{1.6}W\_50$; (c) WY_3W_50; (d) $WY_3W\_W\_50$.

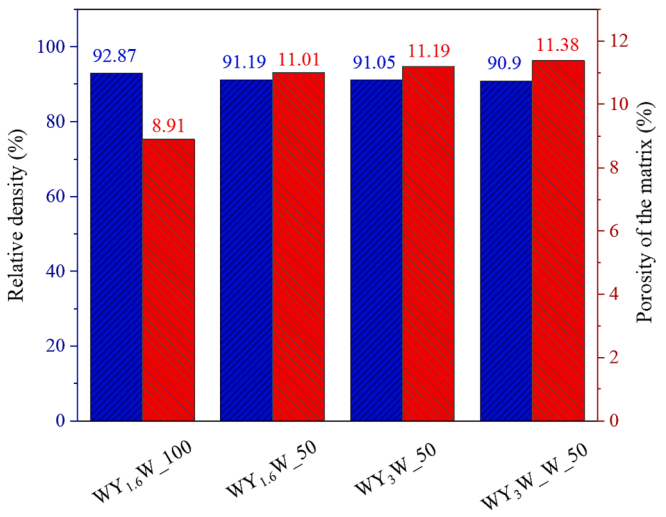

Fig. 6. Relative densities and matrix porosities of the sintered W_f/Y_2O_3/W composites.

section, and the fiber grain size is measured and shown in Fig. 5. It is different from the curled structure grains (in the cross-section) of the as-fabricate fibers [35]. This indicates that the fibers have recovery and recrystallization during FAST [14]. After measuring all grains shown in Fig. 5, the statistics of the fiber grain size shows that the sample $WY_{1.6}W\_100$ has a larger grain size (in range of 0.8–4 μm) than the other samples (in the range of 0.3–3 μm). And the size of the matrix grains has the similar relationship. It indicates that the higher heating rate could accelerate recrystallization and grain growth of the fibers. The Y_2O_3 layer has a protection on the microstructure of the fibers during the FAST process [34], but it shows little effect on it in the present work by comparing $WY_{1.6}W\_50$, WY_3W_50 and $WY_3W\_W\_50$.

The measured relative densities of all prepared samples are shown in Fig. 6. The relative densities are slightly varying. The $WY_{1.6}W\_100$ shows the highest relative density of 92.87%, and the values decrease with the increase of the integrity of the Y_2O_3 interface. The porosity of the samples is mainly contributed by the matrix due to the dense structure of the W-fibers. The porosity of the matrix in each sample is calculated according to [39]:

$$p = V_f p_f + V_m p_m \tag{4.1}$$

where, p, p_f and p_m are the porosity of the composite, fiber and matrix, respectively. V_f and V_m are the volume fraction of fibers and matrix (20% and 80% respectively in this work). The similar porosity of the prepared samples proves that the Y_2O_3 coating and heating rate have little effect on the composite density in this work.

The microstructure of the fibers in the longitudinal section shows that the fibers in all samples have a high aspect ratio (as shown in Fig. 7), which is different from the fibers without Y_2O_3 coating reported in [34]. Same to the morphology in the cross-section, there is no Y_2O_3 layer in $WY_{1.6}W\_100$ (Fig. 7a), and the integrity of the Y_2O_3 layer increases in the order of $WY_{1.6}W\_50$ (Fig. 7b), WY_3W_50 (Fig. 7c) and $WY_3W\_W\_50$ (Fig. 7d). Moreover, a layer of CVD-W can be observed in $WY_3W\_W\_50$. The fiber grain of $WY_{1.6}W\_100$ has the larger size than that of the other three samples.

As mentioned above, the $WY_{1.6}W\_100$ has the larger grain size in both the fiber and the matrix, and there is no Y_2O_3 layer at the fiber–matrix interface (Fig. 8a). It indicates that the higher heating rate could accelerate the process of grain growth and the damage of the Y_2O_3 layer. Fig. 8b illustrates the microstructure of the matrix in the vicinity of the fiber, and the corresponding distribution of each element is shown in Fig. 8c–e. The pores in the matrix are the residue of the gaps between W particles during the sintering process, thus they distribute at the boundary between different W particles instead of in the particles. In

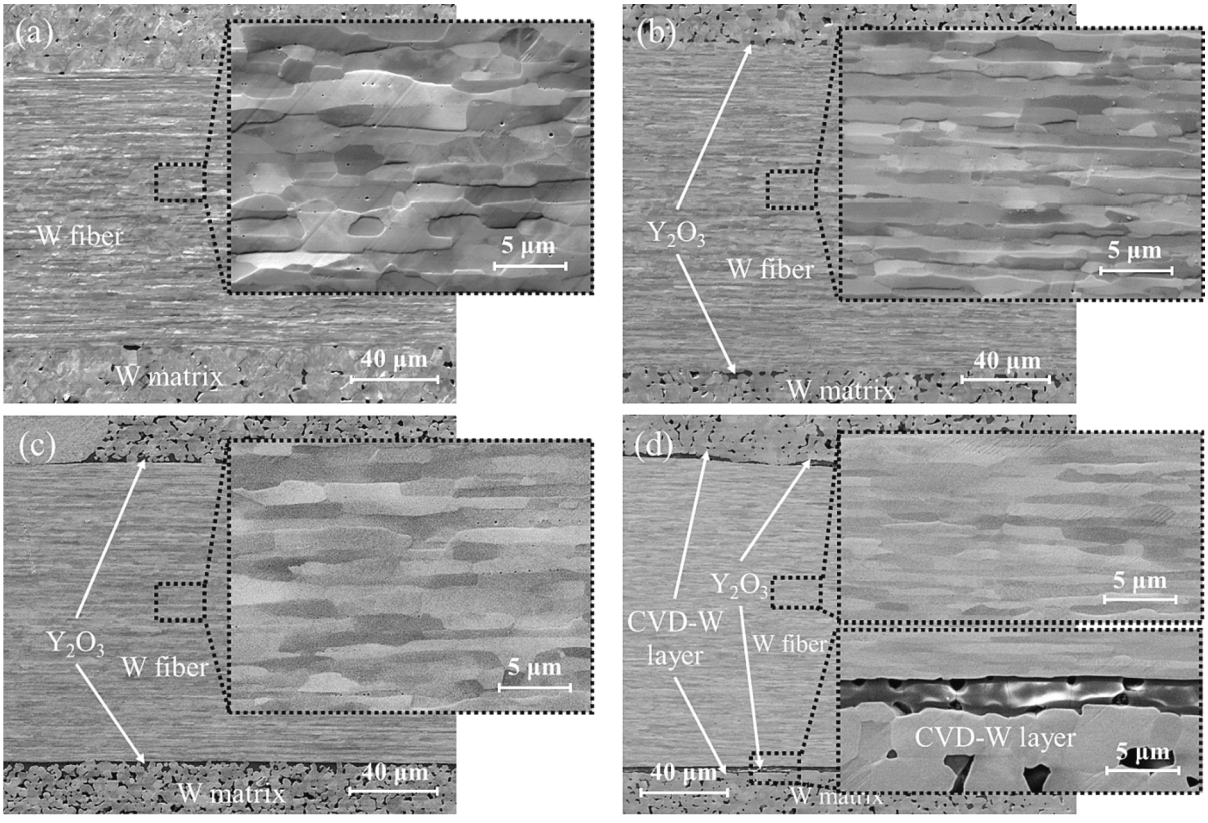

Fig. 7. Microstructure of the longitudinal section of the W fiber: (a) $WY_{1.6}W\_100$; (b) $WY_{1.6}W\_50$; (c) WY_3W_50; (d) $WY_3W\_W\_50$.

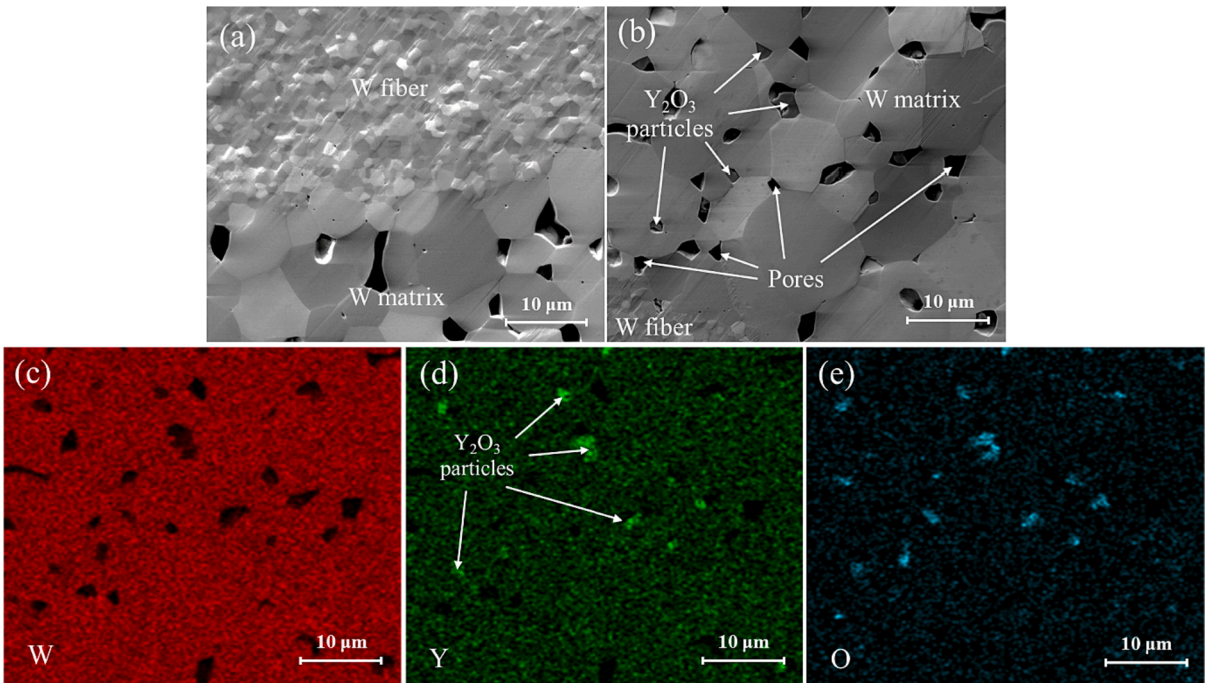

Fig. 8. (a) Microstructure of the fiber–matrix interface in $WY_{1.6}W\_100$; (b) Microstructure of the matrix in the vicinity of the fiber in $WY_{1.6}W\_100$ and (c-e) the corresponding distributions of the elements W, Y and O by EDX mapping analysis.

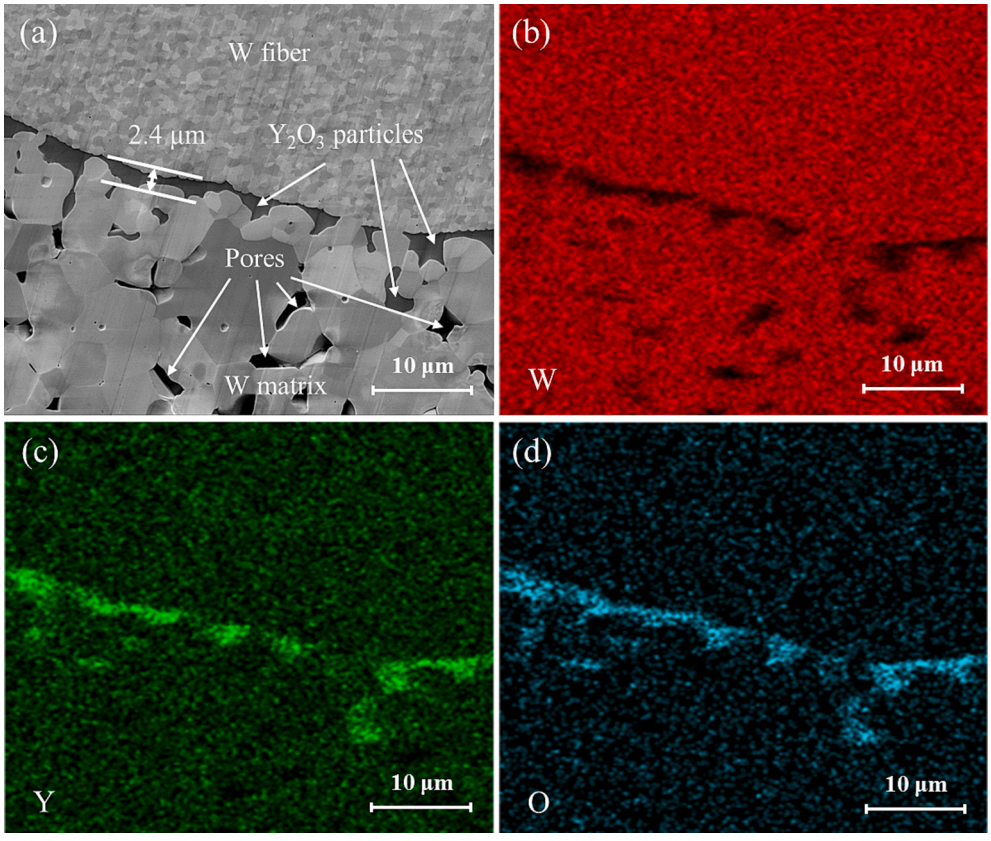

Fig. 9. (a) Microstructure of the interface region in $WY_{1.6}W\_50$ and (b-d) the corresponding distributions of the elements W, Y and O by EDX mapping analysis.

addition, the Y_2O_3 particles in various shapes and sizes are embedded in some of the pores.

Different from the $WY_{1.6}W\_100$, the Y_2O_3 layer still exists at the fiber–matrix interface in $WY_{1.6}W\_50$ although the structure is discontinuous (details are shown in Fig. 9). The thickness of Y_2O_3 layer at different location shows some difference and there are some areas without any interlayer. The measured thickness of the Y_2O_3 layer is 2.4 ± 0.6 μm (by measuring 10 randomly selected positions) which is

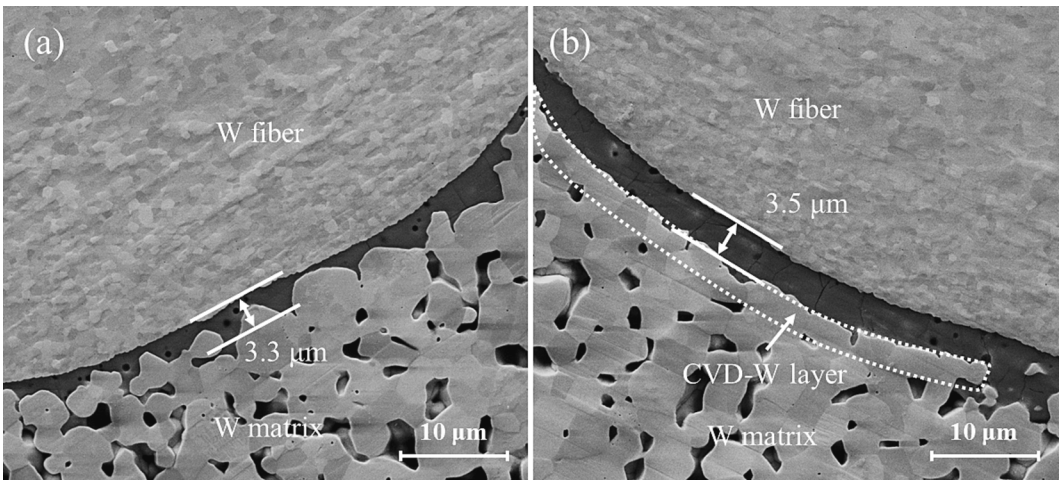

Fig. 10. Microstructure of the fiber–matrix interface: (a) WY_3W_50; (b) $WY_3W\_W\_50$.

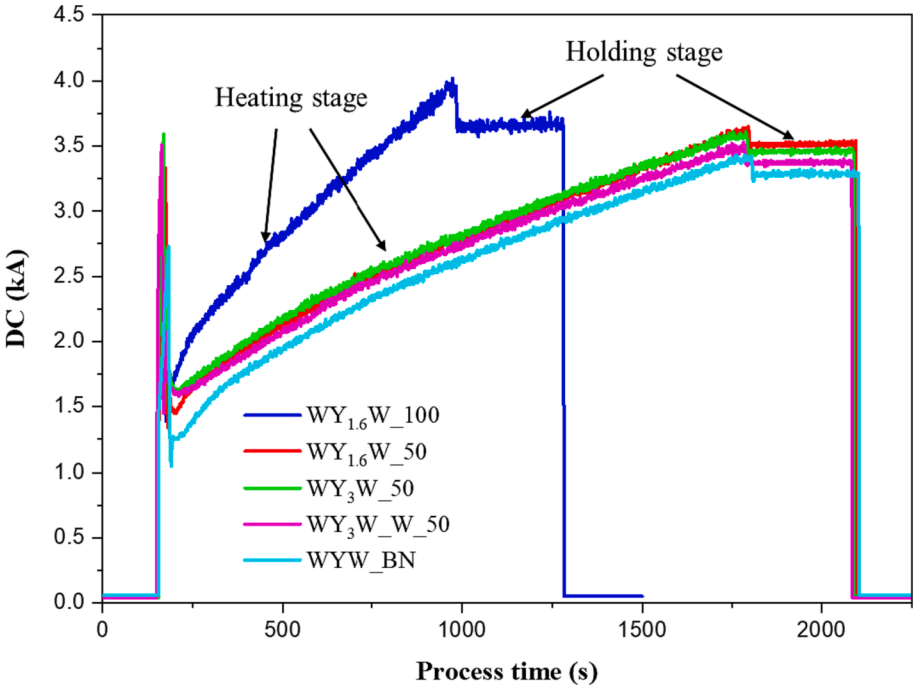

Fig. 11. Evolution of the current intensity with time during the FAST process.

thicker than the original coated thickness (≈1.6 μm). The boundary between the fiber and the Y_2O_3 layer is flat, while a jagged boundary exists between the matrix and the Y_2O_3 layer. Except for the Y_2O_3 layer between the fiber and the matrix, there are also some Y_2O_3 particles embedded in the adjacent matrix. The fabrication parameters are the same between $WY_{1.6}W\_100$ and $WY_{1.6}W\_50$, except for the heating rate.

The Y_2O_3 interface in WY_3W_50 (with the thickness of 3.3 ± 0.3 μm, as shown in Fig. 10a) has the same shape with $WY_{1.6}W\_50$ (2.4 ± 0.6 μm, as shown in Fig. 9a), although it is a little thicker due to the thicker original Y_2O_3 coating of the former. As shown in Fig. 10b, the integrity of the Y_2O_3 layer in $WY_3W\_W\_50$ (with the thickness of 3.5 ± 0.1 μm) is much better than the other samples due to the protection of the CVD-W layer. The boundary between the Y_2O_3 layer and the matrix is continuous and flat, which is different from the other layers without CVD-W, as shown in Fig. 9a within the zigzag-shape structures. The increase of the thickness of Y_2O_3 layer zone also occurs in this sample, which indicates that the Y_2O_3 layer also faced some damage during the FAST process despite the protection of the CVD-W layer. This indicates that the thickness of the protection CVD-W layer needs to be adjusted.

The heating rate is mainly controlled by the current during the FAST process and the different coating states may have some effects on the conductivity of the samples [19,40]. Therefore, it is speculated that the current intensity is the main sintering parameter affecting the microstructure of the composites in the present work. Fig. 11 shows the evolution of the current intensity over process time of each sample during the FAST process. After a sharp peak at the beginning, the samples enter the stable heating stage, where the current gradually increases from ≈1.5 kA with a decreased slope. The current of $WY_{1.6}W\_100$ is higher than the other samples and the slope of it is almost twice higher than the other samples. The higher current could cause the more serious damage to the Y_2O_3 layer [34]. At the end of heating, the current has a drop and keeps constant to the stage of 5 min holding time. The $WY_{1.6}W\_100$ shows the highest value (3.65 kA) at the holding stage, and the others decrease in the order of $WY_{1.6}W\_50$ (3.52 kA), WY_3W_50 (3.46 kA) and $WY_3W\_W\_50$ (3.36 kA). It indicates that the current during the FAST process is related to the electrical resistance of the

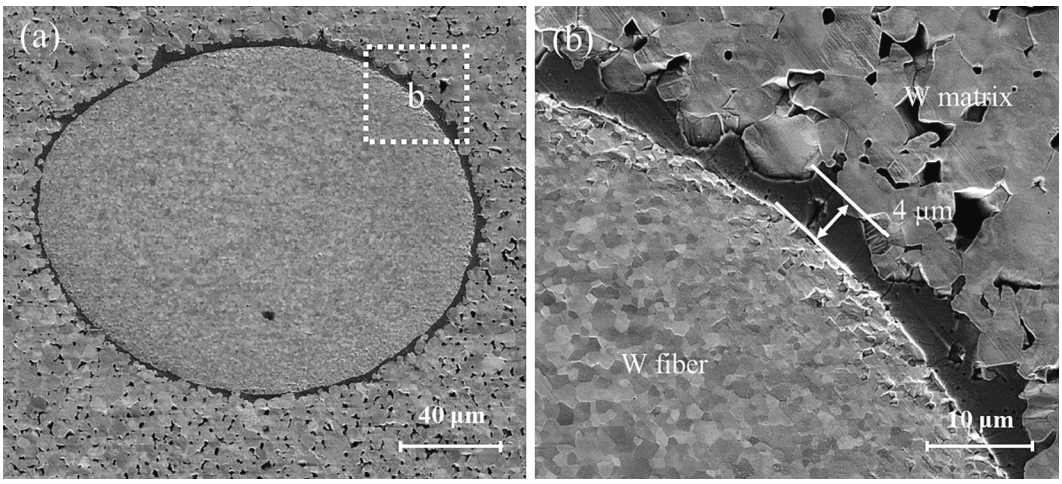

Fig. 12. Microstructure of the WYW_BN composite: (a) a representative fiber; (b) the fiber–matrix interface.

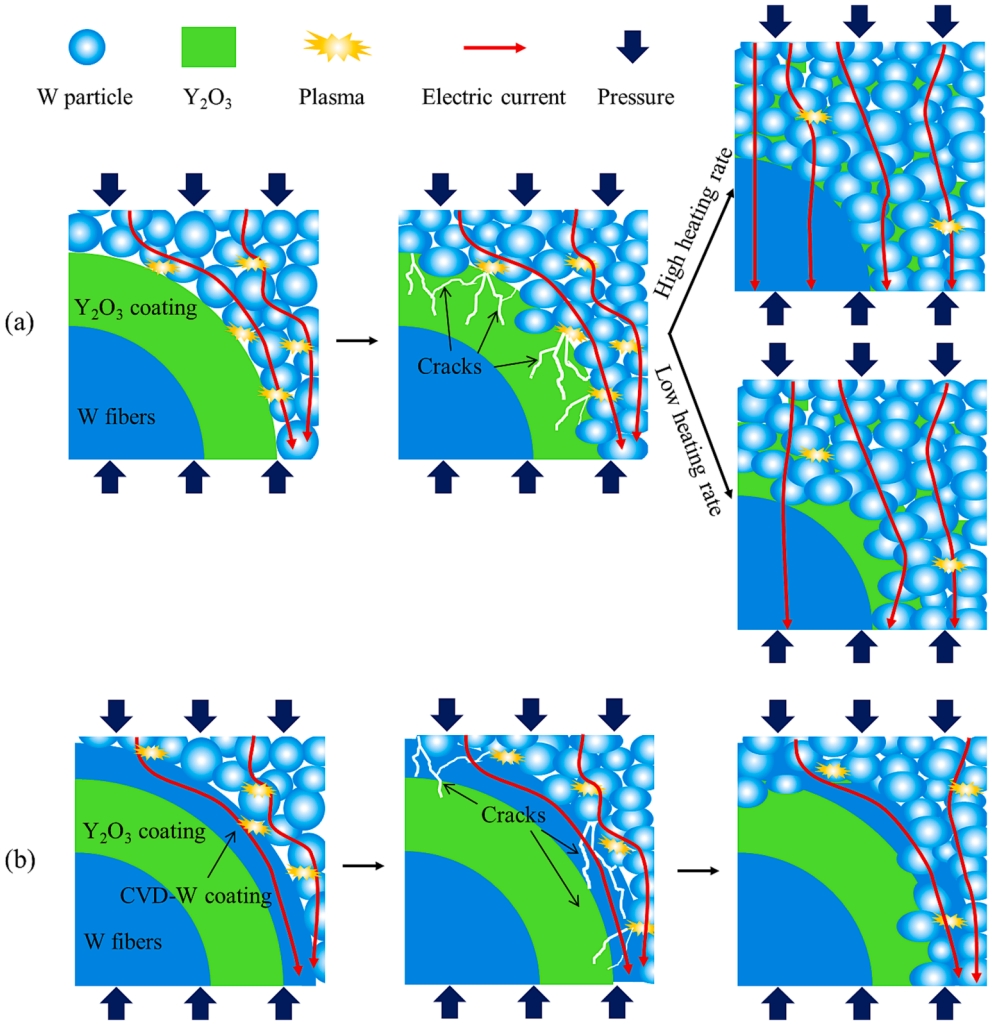

Fig. 13. Diagrams of the evolution of the interface region in $W_f/Y_2O_3/W$ composites during the FAST process: (a) without CVD-W coating [34]; (b) with CVD-W coating.

sample [41]. The currents at the holding stage are well consistent with the integrity of the Y_2O_3 layer of the samples. The better integrity leads to the higher electrical resistance due to the Y_2O_3 is electrically isolating [42]. This phenomenon also proves that the current is able to flow through the fibers after the Y_2O_3 layer is damaged [34].

In addition, an additional sample (WYW_BN) is sintered, utilizing an isolating layer of Biron Nitride (BN) coating on the graphite sheets. Since BN is electrically insulating, the current mainly flows through the mold but not the sample with the aim to eliminate the effect of the current [43,44]. The current of the sintering process of WYW_BN shows the

lowest value (as shown in Fig. 11), and the current flowing through the sample is significantly decreased. As shown in Fig. 12, the thickness of the fiber–matrix interface in the WYW_BN sample after sintering is 4 ± 0.3 μm (the original Y_2O_3 coating is ≈3 μm), which indicates that the Y_2O_3 interface is still damaged. However, its interface shows better continuity than that in WY_3W_50 (Fig. 10a). This proves the previous hypothesis that the current will accelerate the damage of the fiber–matrix interface.

Fig. 13 illustrates the diagrams of the evolution of the interface region in $W_f/Y_2O_3/W$ composites during the FAST process. The Y_2O_3 coating produced by the magnetron sputtering is a stable cubic phase [33]. Therefore, the disappearance of Y_2O_3 coating could be considered as a physical process (The continuous Y_2O_3 coating damaged into small particles, which moves and disperses into the adjacent matrix.). The damage of the Y_2O_3 coating is caused by the high pressure and temperature, as well as the plasma and the local Joule heating formed at the contact surface based on the pulsed current [45–47]. The process has been discussed in [34]. As shown in Fig. 13a, if the coating is completely damaged before the end of sintering process, the current will flow though the fiber and further accelerate the process of grain growth. With the protection of CVD-W layer, the damage of Y_2O_3 coating is reduced (Fig. 13b).

The elevated heating rate, in tandem with an accelerated pressurization rate, results in an increased densification rate. This sequence of events contributes to more pronounced impairment of the Y_2O_3 layer. Concurrently, the Y_2O_3 particles, compromised by this process, are susceptible to simultaneous movement with the tungsten particles. The higher heating rate is accompanied by a higher pressurization rate, leading to the higher densification rate, which causes the more serious damage to the Y_2O_3 layer. However, the inclusion of a protective layer atop the Y_2O_3 layer within the WY_3W_W_50 composition may mitigate the extent of damage incurred during these operations.

4. Conclusion and outlook

The continuous fiber reinforced $W_f/Y_2O_3/W$ composites were fabricated via field assisted sintering technology. The influence of the heating rate and Y_2O_3 coating on the microstructure of the composites were analyzed by comparing the microstructure of the samples prepared under different heating rate and Y_2O_3 coating. The $WY_{1.6}W$_100 sample shows the largest grain size and there is no Y_2O_3 layer existing at the fiber–matrix interface. It indicates that a high heating rate may accelerate the destruction to the Y_2O_3 coating which then leads to current flow through the W fibers. The current causes the heating of the fibers and thus causes recrystallization and grain growth of the fibers. The longer coating time is conducive to the retention of the Y_2O_3 coating after sintering. The CVD-W layer has the potential to shield the Y_2O_3 coating from damage effectively. Nonetheless, further research is required to ascertain the optimal thickness of the CVD-W layer for maximum protection. Detailed analysis of the Y_2O_3 coating properties, alongside the refinement of sintering parameters, will be pursued in future work.

CRediT authorship contribution statement

Rui Shu: Writing – review & editing, Writing – original draft, Investigation, Conceptualization. **Yiran Mao:** Supervision, Methodology, Investigation, Conceptualization. **Alexander Lau:** Methodology, Investigation. **Jan W Coenen:** Validation, Supervision. **Alexis Terra:** Methodology, Investigation. **Chao Liu:** Investigation. **Johann Riesch:** Resources, Investigation, Conceptualization. **Christian Linsmeier:** Resources, Project administration, Funding acquisition. **Christoph Broeckmann:** Resources, Project administration.

Declaration of Competing Interest

The authors declare that they have no known competing financial interests or personal relationships that could have appeared to influence the work reported in this paper.

Data availability

No data was used for the research described in the article.

Acknowledgements

This work has been carried out within the framework of the EUROfusion Consortium, funded by the European Union via the Euratom Research and Training Programme (Grant Agreement No 101052200 - EUROfusion). Rui Shu is financially supported by China Scholarship Council (CSC) with No. 202007000034. Views and opinions expressed are however those of the author(s) only and do not necessarily reflect those of the European Union or the European Commission. Neither the European Union nor the European Commission can be held responsible for them.

References

[1] Y.H. Zhang, W.Z. Han, Mechanism of brittle-to-ductile transition in tungsten under small-punch testing, Acta Mater. 220 (2021) 117332, https://doi.org/10.1016/J.ACTAMAT.2021.117332.
[2] X.F. Xie, Z.M. Xie, R. Liu, Q.F. Fang, C.S. Liu, W.Z. Han, X. Wu, Hierarchical microstructures enabled excellent low-temperature strength-ductility synergy in bulk pure tungsten, Acta Mater. 228 (2022) 117765, https://doi.org/10.1016/J.ACTAMAT.2022.117765.
[3] S. Nogami, S. Watanabe, J. Reiser, M. Rieth, S. Sickinger, A. Hasegawa, A review of impact properties of tungsten materials, Fusion Eng. Des. 135 (2018) 196–203, https://doi.org/10.1016/j.fusengdes.2018.08.001.
[4] C. Ren, Z.Z. Fang, M. Koopman, B. Butler, J. Paramore, S. Middlemas, Methods for improving ductility of tungsten - A review, Int. J. Refract Metal Hard Mater. 75 (2018) 170–183.
[5] Y. Mao, J.W. Coenen, J. Riesch, S. Sistla, C. Chen, Y. Wu, L. Raumann, R. Neu, C. Linsmeier, C. Broeckmann, Spark plasma sintering produced W-fiber-reinforced tungsten composites, Spark Plasma Sinter, Mater. Adv. Process. Appl. (2019) 239–261, https://doi.org/10.1007/978-3-030-05327-7.
[6] L.H. Zhang, Y. Jiang, Q.F. Fang, T. Zhang, X.P. Wang, C.S. Liu, Toughness and microstructure of tungsten fibre net-reinforced tungsten composite produced by spark plasma sintering, Mater. Sci. Eng. A 659 (2016) 29–36, https://doi.org/10.1016/j.msea.2016.02.034.
[7] Y. Mao, J. Coenen, S. Sistla, C. Liu, A. Terra, X. Tan, J. Riesch, T. Hoeschen, Y. Wu, C. Broeckmann, C. Linsmeier, Design of tungsten fiber-reinforced tungsten composites with porous matrix, Mater. Sci. Eng. A 817 (2021) 141361, https://doi.org/10.1016/j.msea.2021.141361.
[8] J. Riesh, M. Aumann, J.W. Coenen, H. Gietl, G. Holzner, T. Höschen, P. Huber, M. Li, C. Linsmeier, R. Neu, Chemically deposited tungsten fibre-reinforced tungsten – The way to a mock-up for divertor applications, Nucl. Mater. Energy. 9 (2016) 75–83, https://doi.org/10.1016/j.nme.2016.03.005.
[9] H. Gietl, J. Riesch, J.W. Coenen, T. Höschen, C. Linsmeier, R. Neu, Tensile deformation behavior of tungsten fibre-reinforced tungsten composite specimens in as-fabricated state, Fusion Eng. Des. 124 (2017) 396–400, https://doi.org/10.1016/j.fusengdes.2017.02.054.
[10] J.W. Coenen, Y. Mao, S. Sistla, J. Riesch, T. Hoeschen, C. Broeckmann, R. Neu, C. Linsmeier, Improved pseudo-ductile behavior of powder metallurgical tungsten short fiber-reinforced tungsten (W_f/W), Nucl. Mater. Energy. 15 (2018) 214–219, https://doi.org/10.1016/j.nme.2018.05.001.
[11] J. Riesch, J. Almanstötter, J.W. Coenen, M. Fuhr, H. Gietl, Y. Han, T. Höschen, C. Linsmeier, N. Travitzky, P. Zhao, R. Neu, Properties of drawn W wire used as high performance fibre in tungsten fibre-reinforced tungsten composite, IOP Conf. Ser. Mater. Sci. Eng. 139 (2016), https://doi.org/10.1088/1757-899X/139/1/012043.
[12] J. Riesch, A. Feichtmayer, M. Fuhr, J. Almanstötter, J.W. Coenen, H. Gietl, T. Höschen, C. Linsmeier, R. Neu, Tensile behaviour of drawn tungsten wire used in tungsten fibre-reinforced tungsten composites, Phys. Scr. 2017 (2017), https://doi.org/10.1088/1402-4896/aa891d.
[13] J. Riesch, Y. Han, J. Almanstötter, J.W. Coenen, T. Höschen, B. Jasper, P. Zhao, C. Linsmeier, R. Neu, Development of tungsten fibre-reinforced tungsten composites towards their use in DEMO - Potassium doped tungsten wire, Phys. Scr. 2016 (2016) 14006, https://doi.org/10.1088/0031-8949/T167/1/014006.
[14] P. Zhao, J. Riesch, T. Höschen, J. Almanstötter, M. Balden, J.W. Coenen, R. Himml, W. Pantleon, U. von Toussaint, R. Neu, Microstructure, mechanical behaviour and fracture of pure tungsten wire after different heat treatments, Int. J. Refract Metal Hard Mater. 68 (2017) 29–40, https://doi.org/10.1016/j.ijrmhm.2017.06.001.

[15] Y. Mao, J.W. Coenen, J. Riesch, S. Sistla, J. Almanstötter, B. Jasper, A. Terra, T. Höschen, H. Gietl, C. Linsmeier, C. Broeckmann, Influence of the interface strength on the mechanical properties of discontinuous tungsten fiber-reinforced tungsten composites produced by field assisted sintering technology, Compos. A Appl. Sci. Manuf. 107 (2018) 342–353, https://doi.org/10.1016/j.compositesa.2018.01.022.
[16] Y. Mao, J.W. Coenen, J. Riesch, S. Sistla, J. Almanstötter, B. Jasper, A. Terra, T. Höschen, H. Gietl, M. Bram, J. Gonzalez-Julian, C. Linsmeier, C. Broeckmann, Development and characterization of powder metallurgically produced discontinuous tungsten fiber reinforced tungsten composites, Phys. Scr. 2017 (2017), https://doi.org/10.1088/0031-8949/2017/T170/014005.
[17] B. Jasper, J.W. Coenen, J. Riesch, T. Höschen, M. Bram, C. Linsmeier, Powder metallurgical tungsten fiber-reinforced tungsten, Mater. Sci. Forum 825–826 (2015) 125–133, https://doi.org/10.4028/www.scientific.net/MSF.825-826.125.
[18] Z.H. Zhang, Z.F. Liu, J.F. Lu, X.B. Shen, F.C. Wang, Y.D. Wang, The sintering mechanism in spark plasma sintering - Proof of the occurrence of spark discharge, Scr. Mater. 81 (2014) 56–59, https://doi.org/10.1016/j.scriptamat.2014.03.011.
[19] S.X. Song, Z. Wang, G.P. Shi, Heating mechanism of spark plasma sintering, Ceram. Int. 39 (2013) 1393–1396, https://doi.org/10.1016/j.ceramint.2012.07.080.
[20] X.P. Li, M. Yan, H. Imai, K. Kondoh, G.B. Schaffer, M. Qian, The critical role of heating rate in enabling the removal of surface oxide films during spark plasma sintering of Al-based bulk metallic glass powder, J. Non Cryst. Solids 375 (2013) 95–98, https://doi.org/10.1016/j.jnoncrysol.2013.05.001.
[21] A. Mondal, A. Upadhyaya, D. Agrawal, Effect of heating mode on sintering of tungsten, Int. J. Refract Metal Hard Mater. 28 (2010) 597–600, https://doi.org/10.1016/j.ijrmhm.2010.05.002.
[22] K. Cui, Y. Zhang, T. Fu, J. Wang, X. Zhang, Toughening mechanism of mullite matrix composites: a review, Coatings 10 (2020), https://doi.org/10.3390/coatings10070672.
[23] R. Shu, Y. Mao, J.W. Coenen, A. Terra, C. Liu, S. Schönen, J. Riesch, C. Linsmeier, C. Broeckmann, Interface and mechanical properties of the ssingle-layer long fiber reinforced W_f/W composites fabricated via field assisted sintering technology, Mater. Sci. Eng. A 857 (2022), https://doi.org/10.1016/j.msea.2022.144098.
[24] J.P. Singh, D. Singh, M. Sutaria, Ceramic composites: roles of fiber and interface, Compos. A Appl. Sci. Manuf. 30 (1999) 445–450, https://doi.org/10.1016/S1359-835X(98)00133-X.
[25] J. Du, T. Höschen, M. Rasinski, S. Wurster, W. Grosinger, J.H. You, Feasibility study of a tungsten wire-reinforced tungsten matrix composite with ZrOx interfacial coatings, Compos. Sci. Technol. 70 (2010) 1482–1489, https://doi.org/10.1016/j.compscitech.2010.04.028.
[26] J. Du, T. Höschen, M. Rasinski, J.H. You, Interfacial fracture behavior of tungsten wire/tungsten matrix composites with copper-coated interfaces, Mater. Sci. Eng. A 527 (2010) 1623–1629, https://doi.org/10.1016/j.msea.2009.10.046.
[27] H. Gietl, S. Olbrich, J. Riesch, G. Holzner, T. Höschen, J.W. Coenen, R. Neu, Estimation of the fracture toughness of tungsten fibre-reinforced tungsten composites, Eng. Fract. Mech. 232 (2020) 107011, https://doi.org/10.1016/j.engfracmech.2020.107011.
[28] F.W. Zok, C.G. Levi, Mechanical properties of porous-matrix ceramic composites, Adv. Eng. Mater. 3 (2001) 15–23, https://doi.org/10.1002/1527-2648(200101)3:1/2<15::AID-ADEM15>3.0.CO;2-A.
[29] Y. Mao, J.W. Coenen, S. Sistla, X. Tan, J. Riesch, L. Raumann, D. Schwalenberg, T. Höschen, C. Chen, Y. Wu, C. Broeckmann, C. Linsmeier, Development of tungsten fiber-reinforced tungsten with a porous matrix, Phys. Scr. 2020 (2020), https://doi.org/10.1088/1402-4896/ab482e.
[30] W. Hu, Q. Ma, Z. Ma, Y. Huang, Z. Wang, Y. Liu, Ultra-fine W-Y_2O_3 composite powders prepared by an improved chemical co-precipitation method and its interface structure after spark plasma sintering, Tungsten. 1 (2019) 220–228, https://doi.org/10.1007/s42864-019-00021-w.
[31] G. Yao, X. Liu, Z. Zhao, L. Luo, J. Cheng, X. Zan, Z. Wang, Q. Xu, Y. Wu, Excellent performance of W-Y_2O_3 composite via powder process improvement and Y_2O_3 refinement, Mater. Des. 212 (2021) 110249, https://doi.org/10.1016/j.matdes.2021.110249.
[32] P. Lei, W. Leroy, B. Dai, J. Zhu, X. Chen, J. Han, D. Depla, Study on reactive sputtering of yttrium oxide: process and thin film properties, Surf. Coatings Technol. 276 (2015) 39–46, https://doi.org/10.1016/j.surfcoat.2015.06.052.
[33] Y. Mao, J. Engels, A. Houben, M. Rasinski, J. Steffens, A. Terra, C. Linsmeier, J. W. Coenen, The influence of annealing on yttrium oxide thin film deposited by reactive magnetron sputtering: process and microstructure, Nucl. Mater. Energy. 10 (2017) 1–8, https://doi.org/10.1016/j.nme.2016.12.031.
[34] R. Shu, Y. Mao, J.W. Coenen, A. Terra, C. Liu, S. Schönen, T. Höschen, J. Riesch, C. Linsmeier, C. Broeckmann, Microstructure and mechanical properties of W_f/W composites influenced by Y_2O_3 coating, Int. J. Refract Metal Hard Mater. 115 (2023) 106322, https://doi.org/10.1016/J.IJRMHM.2023.106322.
[35] V. Nikolić, J. Riesch, R. Pippan, The effect of heat treatments on pure and potassium doped drawn tungsten wires: part I - Microstructural characterization, Mater. Sci. Eng. A 737 (2018) 422–433, https://doi.org/10.1016/j.msea.2018.09.027.
[36] H. Gietl, A.V. Müller, J.W. Coenen, M. Decius, D. Ewert, T. Höschen, P. Huber, M. Milwich, J. Riesch, R. Neu, Textile preforms for tungsten fibre-reinforced composites, J. Compos. Mater. 52 (2018) 3875–3884, https://doi.org/10.1177/0021998318771149.
[37] A. Lau, J.W. Coenen, D. Schwalenberg, Y. Mao, T. Höschen, J. Riesch, L. Raumann, M. Treitz, H. Gietl, A. Terra, B. Göhts, C. Linsmeier, K. Theis-Bröhl, J. Gonzalez-Julian, Bulk tungsten fiber-reinforced tungsten (W_f/W) composites using yarn-based textile preforms, J. Nucl. Eng. 4 (2023) 375–390, https://doi.org/10.3390/jne4020027.
[38] Y. Mao, J.W. Coenen, C. Liu, A. Terra, X. Tan, J. Riesch, T. Höschen, Y. Wu, C. Broeckmann, C. Linsmeier, Powder metallurgy produced aligned long tungsten fiber reinforced tungsten composites, J. Nucl. Eng. 3 (2022) 446–452, https://doi.org/10.3390/jne3040030.
[39] C.T. Herakovich, Mechanics of composites: a historical review, Mech. Res. Commun. 41 (2012) 1–20, https://doi.org/10.1016/j.mechrescom.2012.01.006.
[40] D. Tiwari, B. Basu, K. Biswas, Simulation of thermal and electric field evolution during spark plasma sintering, Ceram. Int. 35 (2009) 699–708, https://doi.org/10.1016/j.ceramint.2008.02.013.
[41] C. Romaric, L.G. Sophie, N. Foad, C. Frédéric, B. Guillaume, F. Gilbert, C. Jean-Marc, B. Frédéric, Effect of current on the sintering of pre-oxidized copper powders by SPS, J. Alloy. Compd. 692 (2017) 478–484, https://doi.org/10.1016/j.jallcom.2016.08.191.
[42] C.S. Bonifacio, T.B. Holland, K. Van Benthem, Time-dependent dielectric breakdown of surface oxides during electric-field-assisted sintering, Acta Mater. 63 (2014) 140–149, https://doi.org/10.1016/j.actamat.2013.10.018.
[43] T. Voisin, J.P. Monchoux, A. Couret, Near-net shaping of titanium-aluminum jet engine turbine blades by SPS, (2019), doi: 10.1007/978-3-030-05327-7.
[44] D. Giuntini, J. Raethel, M. Herrmann, A. Michaelis, E.A. Olevsky, D. Bouvard, Advancement of tooling for spark plasma sintering, J. Am. Ceram. Soc. 98 (11) (2015) 3529–3537, https://doi.org/10.1111/jace.13528.
[45] D.M. Hulbert, A. Anders, J. Andersson, E.J. Lavernia, A.K. Mukherjee, A discussion on the absence of plasma in spark plasma sintering, Scr. Mater. 60 (2009) 835–838, https://doi.org/10.1016/j.scriptamat.2008.12.059.
[46] R. Marder, C. Estournès, G. Chevallier, R. Chaim, Plasma in spark plasma sintering of ceramic particle compacts, Scr. Mater. 82 (2014) 57–60, https://doi.org/10.1016/j.scriptamat.2014.03.023.
[47] T.B. Holland, U. Anselmi-Tamburini, D.V. Quach, T.B. Tran, A.K. Mukherjee, Effects of local Joule heating during the field assisted sintering of ionic ceramics, J. Eur. Ceram. Soc. 32 (2012) 3667–3674, https://doi.org/10.1016/j.jeurceramsoc.2012.02.033.